Aeropropulsive Performance Modelling of Over-The-Wing Propulsion at Incidence

Dekker, H.N.J.; Tuinstra, M; Baars, W.J.; Scarano, F.; Ragni, D.

DOI
10.2514/6.2023-3355

Publication date
2023

Document Version
Final published version

Published in
AIAA AVIATION 2023 Forum

AIAA AVIATION Forum
12-16 June 2023, San Diego, CA and Online
AIAA AVIATION 2023 Forum

10.2514/6.2023-3355

Aeropropulsive Performance Modelling of Over-The-Wing Propulsion at Incidence

H.N.J. Dekker[1] and M. Tuinstra[2]
Royal Netherlands Aerospace Centre, Marknesse, Flevoland, 8316 PR, The Netherlands

W.J. Baars[3], F. Scarano[4] and D. Ragni[5]
Delft University of Technology, Delft, Zuid-Holland, 2629 HS, The Netherlands

A semi-emperical model is developed, able to capture the aeropropulsive performance characteristics of Over-The-Wing propellers at incidence. The model is based on an hypothesis on the interactions of the propeller- and wing-induced flow fields. Effects of these interactions on the both the thrust and lift are written in a form in which the dominant design parameters appear explicitly. Both the flow hypothesis and model results are validated using experimental data of a single Over-The-Wing propeller. It is shown that for moderate angles of attack, the propulsive thrust is reduced by the wing's circulation. For angles of attack greater than the stall angle of the isolated wing, thrust is increased by the ingestion of low momentum flow. The propeller is not able to delay stall but induces flow over the wing, which is returned as reduced pressure over the suction side. The model predictions closely match the experimental results for thrust, but integral loading measurements of the wing are required to validate the lift predictions.

I. Nomenclature

a	=	induced velocity factor
B	=	number of blades
BPF	=	Blade Passing Frequency
C	=	wing chord, mm
c_l	=	two-dimensional lift coefficient
c_p	=	two-dimensional pressure coefficient
C_{pow}	=	power coefficient
C_T	=	thrust coefficient
CNC	=	Computer Numerical Control
D_p	=	propeller diameter, mm
J	=	propeller advance ratio
N_p	=	number of propellers
q	=	free-stream dynamic pressure, pa
Q	=	propeller torque, Nm
R	=	radial coordinate
R_0	=	propeller inner radius, mm
R_1	=	propeller outer radius, mm
Re_c	=	chord-based Reynolds number

[1] Ph.D. Candidate, Vertical Flight and Aeroacoustics Department; h.n.j.dekker-1@tudelft.nl. Member AIAA.
[2] Scientist Principal Aeroacoustics, Vertical Flight and Aeroacoustics Department; marthijn.tuinstra@nlr.nl. Member AIAA.
[3] Assistant Professor, Aerodynamics, Faculty of Aerospace Engineering; w.j.baars@tudelft.nl. Senior Member AIAA.
[4] Full Professor, Aerodynamics, Faculty of Aerospace Engineering; f.scarano@tudelft.nl. Member AIAA.
[5] Associate Professor, Wind Energy, Faculty of Aerospace Engineering; d.ragni@tudelft.nl. Member AIAA

S	=	wing span, mm
SPL	=	Sound Pressure Level
T	=	propeller thrust, N
u_e	=	edge velocity, m/s
V_∞	=	free-stream velocity, m/s
x_p	=	propeller x-position, mm
y_p	=	propeller y-position, mm
α	=	free-stream angle of attack, rad
α_{eff}	=	effective angle of attack, rad
α_s	=	stall angle, rad
δ	=	shear layer thickness
θ	=	azimuthal coordinate
ρ	=	density of air, $kg \cdot m^{-3}$
τ	=	tracer particle relaxation time, s
φ	=	blade inflow angle
Ω	=	shaft frequency, Hz

II. Introduction

Urban Air Mobility (UAM) [1] aims at a transportation system that will shorten travel times in metropolitan areas, by enabling air-linked destinations in closer proximity to one another than regular airports. This is achieved by leveraging eVTOL (electric Vertical Take-Off and Landing) configurations, to deploy highly versatile and maneuverable disruptive aircraft systems. Making use of the great scalability characteristics of electric motors, allows for increased design freedom for the propulsion system. Hence, disruptive solutions are discovered [2], resulting in unexplored aerodynamic and aeroacoustic installation effects.

The majority of the current design solutions for UAM vehicles can be placed into four categories: the multi-rotors, lift+cruise concepts, tilt-rotors and tilt-wing vehicles [6,9]. The tilt-wing configurations make use of tiltable wings and propulsors (propellers or fans), to combine take-off and landing flexibility with an efficient forward flight. This creates a complex flight envelope, consisting of vertical take-off, hover, transition and climb before cruise conditions are reached [4]. During the transition phase, the dominant lift force gradually changes from propulsive thrust to the wing's lift. Consequently, the flight conditions are characterized by low advance ratios and high angles of attack, determining wings operating close to stall [6].

Tilt-wing configuration employ multiple propulsors which are positioned in close proximity to the wing to create beneficial aero-propulsive coupling effects [5]. The widely used example of such a layout is the Leading-Edge Distributed Electric Propulsion (LE-DEP), where propellers are installed on pylons connected to the wing's leading edge. Using the induced flow provided downstream of the propellers, LE-DEP is known to increase the lift coefficient of the wing by increasing the dynamic pressure downstream of the disks [12]. Nonetheless, LE-DEP suffers from a few disadvantages. The propellers are operated in non-uniform inflow by the wing's upstream effect [13], resulting in unsteady loading on the propeller blades. Additionally, the propellers are open and the slipstream and tip vortices of the blades impede on the wing's leading edge [14], which creates unfavorable acoustic installation effects.

An alternative is to mount the propulsors over the suction side of the wing, with the propeller's axes aligned with the wing's chord line, as schematically illustrated in Figure 1. By this orientation, labeled as the "Over-The-Wing (OTW) Propeller" or "OTW-DEP", propeller noise is shielded by the wing, which can be used to reduce fly-over noise [15]. Furthermore, similar to the LE-DEP, flow is induced over the wing. However, here only the suction side of the wing is predominantly affected, by both the upstream and downstream part of the propellers' stream tubes. This has a favorable effect on the wing's lift production. A lift increase of 8% for the OTW propeller has been shown, caused by both a lift increase and drag reduction compared to the isolated configuration [16]. This lift increase has shown to be sensitive to the chordwise position of the propeller, in which a propeller closer to the trailing edge gave the largest effect on the lift production [20].
In the work of Müller *et al.* [16] and de Vries *et al.* [17] it was shown that the propeller can trigger flow separation when installed upstream of an adverse pressure gradient, as seen with a deflected flap. Contributing to this is both the

adverse pressure gradient imposed by the propeller itself and local axial-velocity deficits, caused by the periodic presence of tip vortices [17].
Apart from the beneficial effects on the lift coefficient of the wing, the propeller performance is adversely affected by the wing's presence. Propulsive efficiency losses of up to 16% have been noted [14]. Furthermore, the wing imposes non-uniform inflow conditions to the propeller resulting in unsteady blade loading. This can result in strong acoustic sources, nullifying the favorable shielding effect.

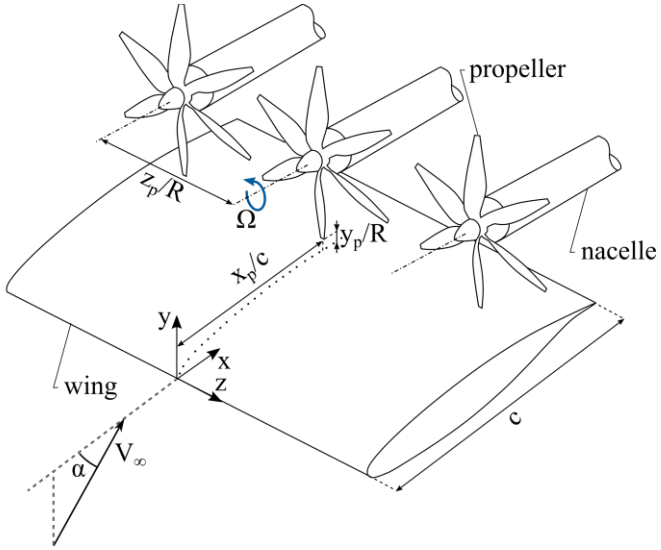

Figure 1. Schematic representation of over-the-wing propulsion with relevant parameters and system of coordinates

The aforementioned studies considered the over-the-wing propeller system either in cruise conditions, or with a detached flap for STOL purposes. Consequently, in these investigations, a moderate angle of attack is considered in advance ratios which are higher compared to the flight regimes typical for eVTOL flight. The high propulsive thrust conditions as seen for the tilt wing vehicles cause a stronger contraction of the stream tube and therefore a more pronounced interaction of the propeller on the wing is expected. This is also seen in the work of Murray *et al*. [21] in which a propeller is positioned over a flat plate and ingests a turbulent boundary layer. In the case with a low advancing flow, a reversal region between the propeller and the plate is formed, similar to the phenomenon behind the formation of ground vortices during runway take-off of turbo-fan [25] and propeller aircraft [26].

Furthermore, in transition and climb flight conditions, angles of attacked that are close to, or over the stall angle are encountered [4]. This positions the propeller in a strong adverse pressure gradient or partially inside a separated boundary layer. It is unclear how this radical change in inflow affects the propeller performance and the corresponding lift enhancement. Information on these installation characteristics and performance trends are required to mitigate the detrimental and maximize the favorable effects.

Hence, in the current study, a hypothesis of flow interactions between the propeller and wing system is proposed, focusing on low advance ratios and high angles of attack. Effects of these flow interactions on both the thrust and lift are estimated to formulate a semi-empirical model, able to capture the trends in aeropropulsive performance. Subsequently, experiments are conducted which serve two purposes. Flow measurements are used to validate the hypotheses made in the semi-empirical model while the integral loading on both the propeller and wing forces allows for comparison between the modelled and measured performance trends. By doing so, hidden installation effects can be identified. The ultimate goal is to provide a better understanding of the performance characteristics of this system architecture during short- and vertical take-off and landing from which design guidelines can be derived.

The outline of the paper is as follows. In chapter III a flow hypothesis is introduced and the semi-empirical model is presented. Chapter IV deals with the experimental setup. The model is then compared and validated with the flow measurements in chapter V. Finally, in chapter VI, the model performance trends are analyzed.

III. Model Description

The propulsion system is approached by decoupling of the wing and propeller system. Hence, the interactions of the isolated wing on the propeller will be given first to determine the relation for thrust.

A. Thrust modelling

The wing changes the inflow towards the propeller, altering the effective advance ratio [22] which is the dominant parameter for propulsive thrust. The (uniform) effective advance ratio J_{eff} is modelled by considering three aerodynamic effects of the isolated wing.

At incidence, the wing will deflect the streamlines of the advancing flow, transferring lateral into axial momentum towards the propeller. Secondly, for small to moderate angles of attack (up to the stall angle) the wing's circulation will increase the axial velocity over the suction side wing. Finally, at large incidence angles, the boundary layer will separate from the wing's leading edge and the propeller will be ingesting low momentum flow. These different contributions are schematically illustrated in Figure 2a. Note that the wing-induced flow field will impose non-axial and non-uniform inflow conditions to the propeller as well. These will primarily impact the acoustic signature and are disregarded in the current analysis, see Figure 2b.

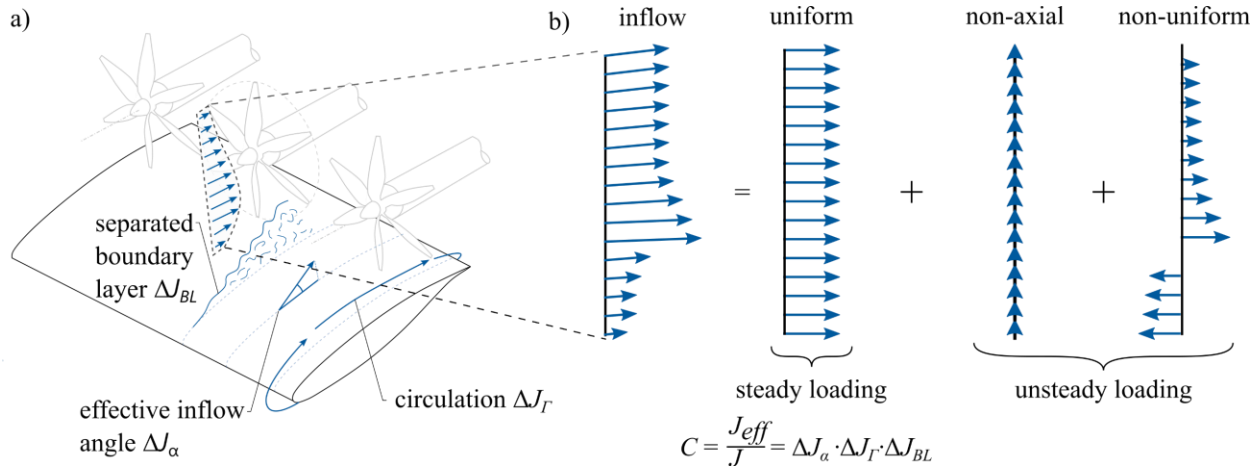

Figure 2 a) Schematic of interactions of the isolated wing on propeller system and b) decomposition of the inflow field

The contributions of each of the aforementioned effects to the corrected advance ratio J_{eff} can briefly be summarized. An effective inflow angle α_{eff} is computed by multiplying the incidence angle with a shape function $\psi_\alpha(x/c)$ depending on the chordwise position over the wing. The shape function $\psi_\alpha(x/c)$ is derived from the flow field around the isolated wing and is aimed to be valid for a wide range of airfoil geometries. Then, by assuming angles below 45º, the contribution of this effect to the advance ratio correction, i.e. ΔJ_α, follows from basic trigonometric relations.

The axial velocity increase by circulation ΔJ_Γ is derived by modelling an edge velocity $U_e(x)$ based on the lift force and Bernoulli's equation, assuming a parabolic lift distribution. The lift force is computed through the Viterna and Corrigan model, which is valid for post-stall conditions [23]. Then, a velocity distribution in y-direction $\psi_y(y)$ is estimated from potential flow analysis around a cylinder with a characteristic length based on the wing's chord c to determine the axial velocity increase at a specific propeller tip gap y/R.

Finally, the contribution of the separated boundary layer ΔJ_{BL} is found by approximating the shear layer as a straight line from the leading edge, tangential to free-stream direction. In the area below the shear line, i.e. in the separated boundary layer, flow velocity is set to 0. The ratio of re-ingestion, is approximated by a logistic function based on the relation of circular segments, normalized by the total area of the propeller disk. To complete the model, a stall criterium is added by using a flow separation angle α_s, as a function of the wing's nose radius to chord length r/c [24].

Contributions of ΔJ_α, ΔJ_Γ & ΔJ_{BL} and are then combined to derive the advance ratio correction factor C ($J_{eff} = J \cdot C$) as presented in equation (1).

$$C = \overbrace{\left(-\frac{1}{2}\alpha^2(2-3x_p)^2+1\right)}^{\Delta J_\alpha}\overbrace{\left(\sqrt{\frac{6(1-x_p{}^2)c^4}{5(y_p+c)^4}c_l+1}\right)}^{\Delta J_\Gamma}\overbrace{\left(\underbrace{\frac{1}{2}\left(\frac{\alpha-\alpha_s}{\sqrt{(\alpha-\alpha_s)^2}}+1\right)}_{Stall\ critium}\underbrace{\left(-2^{-(\delta-y_p+1)^2}+1\right)+1}_{Ratio\ of\ ingestion}\right)}^{\Delta J_{BL}} \tag{1}$$

Neglecting stall on the blades, the propeller thrust coefficient C_T depends linearly on the advance ratio. The slope $\frac{dC_T}{dJ}$ and base $C_{T,h}$ of this relation is specific for each propeller design. Nonetheless, the thrust of the isolated propeller is often known in advance or can be computed with relative ease. Hence, these are defined as variables in equation (2), which presents the relation for thrust coefficient C_T of the installed propeller.

$$C_T = \frac{dC_T}{dJ}JC + C_{T,h} \tag{2}$$

B. Propeller induced velocity

The amount of flow which is induced by the propeller depends on the thrust generated. By representing the propeller as an actuator disk, the induced velocity factor a, which is the induced velocity at the disk normalized by the free-stream velocity, follows directly from equation $a= \frac{1}{2}\left(\frac{\sqrt{16C_T+\pi J}}{\sqrt{\pi}\sqrt{J}}-1\right)$ **(3)** as a function of the (corrected) advance ratio and the thrust coefficient C_T.

$$a = \frac{1}{2}\left(\frac{\sqrt{16C_T+\pi J}}{\sqrt{\pi}\sqrt{J}}-1\right) \tag{3}$$

The induced velocity factor a will be an input for the relation of the lift model. Equation $a= \frac{1}{2}\left(\frac{\sqrt{16C_T+\pi J}}{\sqrt{\pi}\sqrt{J}}-1\right)$ **(3)** therefore serves as the link between the thrust and lift equations.

C. Lift modelling

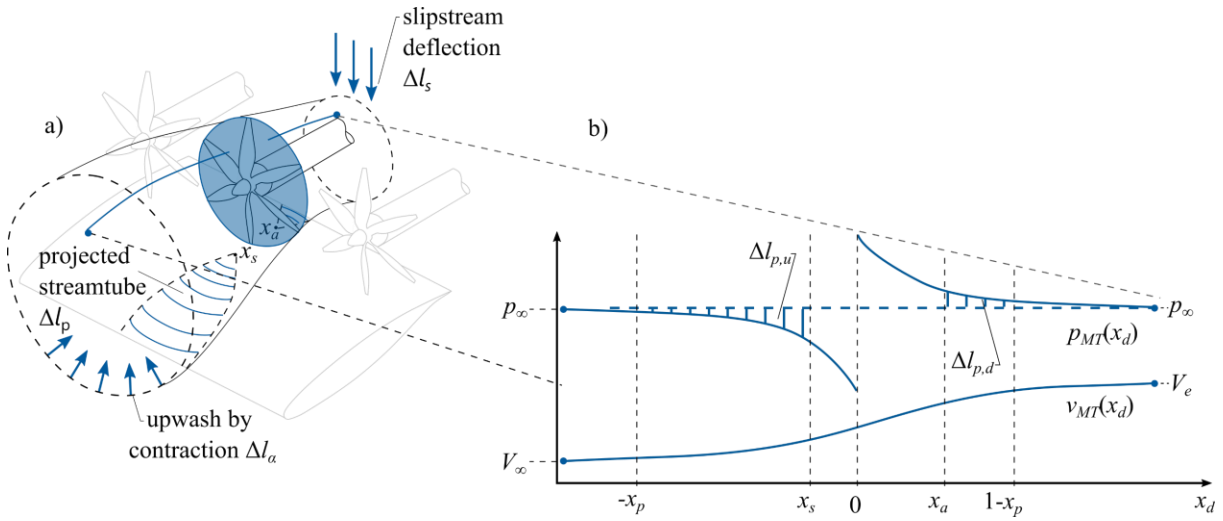

Figure 3 a) Schematic of interactions of the propeller on the wing and b) pressure p_{MT} and axial velocity v_{MT} from momentum theory in the isolated propeller streamtube

The propeller induced flow field causes a threefold of separate aerodynamic effects on the lift production of the wing, which are illustrated in Figure 3a. The pressure along the streamtube varies in the flow direction, see Figure 3b. At the disk a pressure jump occurs (which is proportional to the thrust delivered). When the stream tube attaches to the wing, the combined interaction is represented by the streamtube separation x_s and attachment x_a points in Figure 3a, with a change of the pressure on the wing, resulting in lift difference of $\Delta l_p = \Delta l_{p,u} - \Delta l_{p,d}$, see Figure 3b.
A second aerodynamic effect takes place upstream of the disk. The contraction of the streamtube induces flow in radial direction and creates an effective increase in the angle of attack near the leading edge of the wing, indicated by Δl_α in Figure 3a.
The final aerodynamic effect is the deflection of total stream tube, increasing the circulation of the wing, providing a form of thrust vectoring. This effect is illustrated by Δl_s Figure 3a.

Using the momentum theory and slipstream model for the isolated propeller, relations for the chordwise distribution of the pressure and contraction in the stream tube can be found as a function of a. These can be used to derive a basic equation for the lift coefficient increase Δc_l in a form in which the propeller installation parameters appear explicitly, see equation (4).

$$\Delta c_l = \overbrace{\left(1-\frac{\alpha^2}{2}\right)\frac{\left(\sqrt{a+1}-1\right)y_p N_p}{x_p S}}^{\Delta c_{l,\alpha}} + \overbrace{\left(2-\sqrt{2}\right)a(a+1)\left(\left(2x_p-1\right)c+x_a-x_s\right)}^{\Delta c_{l,pu}-\Delta c_{l,pd}} + \overbrace{\frac{8N_p R_1^2 a^2\left(\frac{1}{2a+1}+1\right)}{S^2}c_{l0}}^{\Delta c_{l,sd}} \tag{4}$$

Here, x_s and x_a denote the attachment and separation points of the streamtube with the wing surface, recall Figure 3. For now, these are set to $0.5R$ upstream and downstream of the propeller disk which closely represent the results of the experimental data.

$$x_s = f(y_p, J, \alpha) \approx x_p/c - 0.5R_1$$

$$x_a = f(y_p, J, \alpha) \approx x_p/c + 0.5R_1$$

D. Limitations of the semi-empirical model

During the analysis of the model a number of assumptions are made which confines the parameter space of the method. An overview of this parameter space, consisting of both geometrical and performance conditions, is provided in Table 1.

Table 1 Parameter space of the aeropropulsive performance model

Free-stream Reynolds number Re_c	> 250,000
Free-stream Mach number M	< 0.3
Advance ratio J	$0.15 \leq J \leq 1.0$
Angle of attack α (º)	$-5 \leq \alpha \leq 45$
Propeller chord wide position x_p/c	$0.2 \leq x_p/c \leq 0.9$
Propeller tip gap y_p	$> \delta_{99}$
Propeller spacing z_p/R	> 1.1 (outside aerodynamic interference)
Propeller radius R	$0.25c \leq R \leq 0.5c$

IV. Experimental setup

A. Wind tunnel

The experiments were performed in the Aeroacoustic Wind tunnel Facility at the Netherlands Aerospace Centre in Marknesse, see Figure 4. The facility consists of an anechoic chamber (9 x 8 x 6 m), yielding an absorption rate of 99% above 200Hz. To increase the quality of the aerodynamic measurements, a closed test section was used, limiting the turbulence intensity to a maximum of 0.01% at a free-stream velocity of 20 m/s.

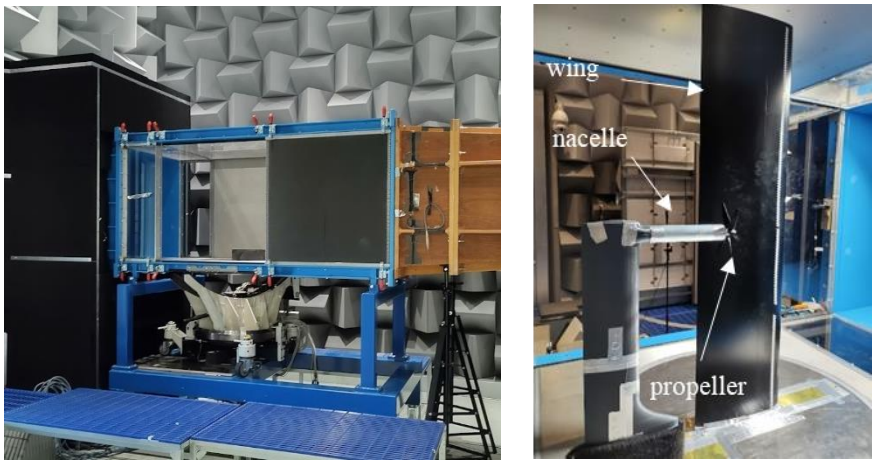

Figure 4 a) Exterior of the test section in the AWT, F15 wing model and nacelle with the propeller in the test section b). Note that one wall has been removed when taking these images.

B. Propeller and wing model

A F15 wing model was mounted vertically on a turntable in the floor of the closed test section, as shown in Figure 2. The chord of the wing comprises 240mm and the boundary layer was tripped at 10% chord on both the suction and pressure side. Over the suction side of the wing, a nacelle was positioned and connected to the same turntable as the wing, with its axis aligned with the wing's chord direction. Inside the nacelle, a brushless in runner motor is connected through a thrust and torque sensor. The motor drives a custom design six-bladed propeller (radius of 63.5 mm) at a shaft frequency of 383 *Hz*. The blade design of this propeller is based on a benchmarked version for low-Reynolds application derived from a NACA4412 airfoil. For additional details on the blade design, the reader is directed to the work of Grande *et al*. [8]. The propeller has been manufactured with CNC out of aluminum with 0.02 mm precision, and cured to avoid material relaxation and oxidation. The measured isolated propeller thrust coefficient C_T and isolated wing lift coefficient c_l are presented in Figure 5.

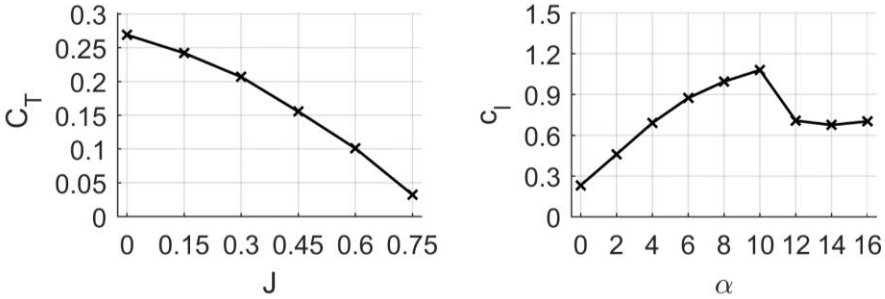

Figure 5 Isolated propeller thrust coefficient C_T as a function of advance ratio (left) and isolated wing c_l-α curve for Re_c = 480,000

A wide range propeller advance ratios J and inflow angles α are investigated for the installed configuration. Furthermore, three different propeller positions along the wing's chord line are considered. The experimental conditions are summarized in Table 2.

Table 2 Over-The-Wing propeller system operating conditions

Wing chord c (mm)	240
Chord Reynolds number Re_c	120,000 – 480,000
Shaft frequency (Hz)	383
Blade Passing Frequency BPF (Hz)	2300
Number of blades B	6
Propeller radius R_1 (mm)	63.5
Propeller tip gap y_p/R	0.27
Propeller chord position x_p/c	[0.3, 0.6, 0.9]
Propeller advance ratio J	[0, 0.15, 0.3, 0.45, 0.6]
Angle of attack α	[0, 2, 4, 6, 8, 10, 12, 14, 16]

C. Measurements techniques

Integral loading

Propeller thrust is measured using a uniaxial FUTEK LSB205 load cell excited with 5 volts of direct current (VDC), which is connected to the motor inside the nacelle. Similarly, torque is measured using a FUTEK QTA141 excited by the same power supply. Repeated measurements showed a maximum deviation of 2% for thrust and 5% for torque.

Pressure orifices

In the center span position of the wing, 59 static pressure taps are fitted. The location of the center span pressure taps along with the contour of the wing profile is presented in Figure 6. Two additional, coarser spaced, pressure tap rows are positioned at 25%- and 75%-span to evaluate the two-dimensionality of the flow. All pressure measurements are averaged over 20 s. For a number of data points, the propeller is traversed along z-direction, in steps of 10 mm to a maximum displacement of 50 mm (0.8 R) in both positive and negative z-direction. This allows for a surface pressure reconstruction to investigate spanwise variations.

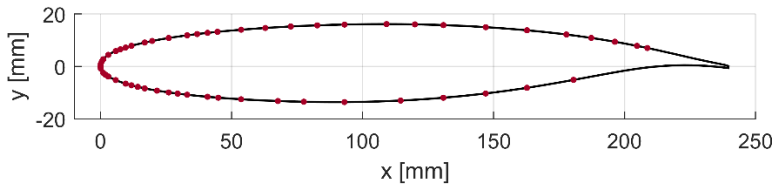

Figure 6 Contour of the F15 wing model with location of the static pressures in the center span indicated by the red dots.

Stereoscopic Particle Image Velocimetry

The flow around the propeller is characterized using stereoscopic particle image velocimetry (sPIV). A schematic of the sPIV setup can be found in Figure 7. The flow is seeded with DEHS tracer particles (τ = 2 µs) which are illuminated by an evergreen laser (200 mJ/pulse) in a sheet of 3mm thickness. Illumination is performed at a rate of 15 Hz and the duration for each pulse (pulse width) is δt = 25 ns. Recording is performed by two sCMOS cameras (*Imager sCMOS CLHS*) placed outside the section at a distance of 0.6 m from the center of the measurement region. The camera is equipped with an objective of focal length f = 50 mm, set at numerical aperture $f_\#$ = 8. The resulting field of view spans 19 x 25 cm^2 (3 R x 4 R). System synchronization is obtained with a LaVision Programmable timing unit (PTU X) and each measurement comprises of at least 300 recordings for a time duration of 20 s. An overview of the illumination and imaging conditions is presented in Table 3.

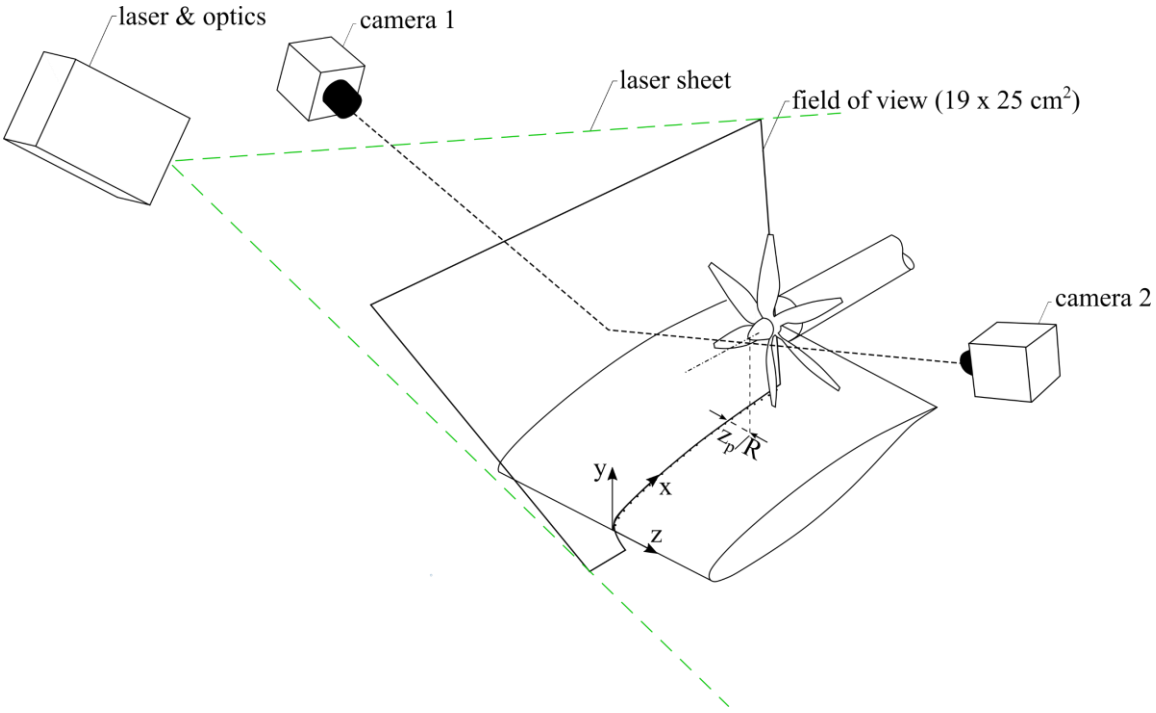

Figure 7 3D schematic of the PIV setup, with coordinate system and field of view.

Table 3 Illumination and imaging conditions

Seeding type	DEHS
Particle relaxation time τ (µs)	2
Illumination	Evergreen (200 mJ/pulse)
Sheet thickness dz (mm)	3
Pulse width δt (ns)	25
Repetition rate (Hz)	15
Camera type	2 x Imager sCMOS CLHS
Camera resolution	2560 x 2160 px^2
Stereo angle	35º
Objective focal length f (mm)	50
Numerical Aperture $f_\#$	8
Optical magnification M	0.009
Field of view (cm^2)	19 x 25
Number of recordings	300
Image analysis	Cross-correlation (32 x 32 px^2)
Vector pitch (mm)	0.6

V. Flow physics

The flow field will be analyzed and compared to the hypothesis of Chapter III by considering three conditions for a constant advance ratio; a zero angle of attack, an angle of attack of 8º which positions the propeller in a strong advance ratio, and the early onset of stall, where a separated boundary layer ingestion is ingested. Wing and propeller induced effects will be examined separately.

A. Wing induced effects

Wing induced effects on propeller performance are modelled through the advance ratio correction factor C. This term is validated using the PIV measurements around the isolated wing. The lines in Figure 8 present the chordwise

distribution of the axial velocity over the suction side compared to free-stream conditions, while the contours are the model prediction for different chordwise propeller positions and angles of attack α.

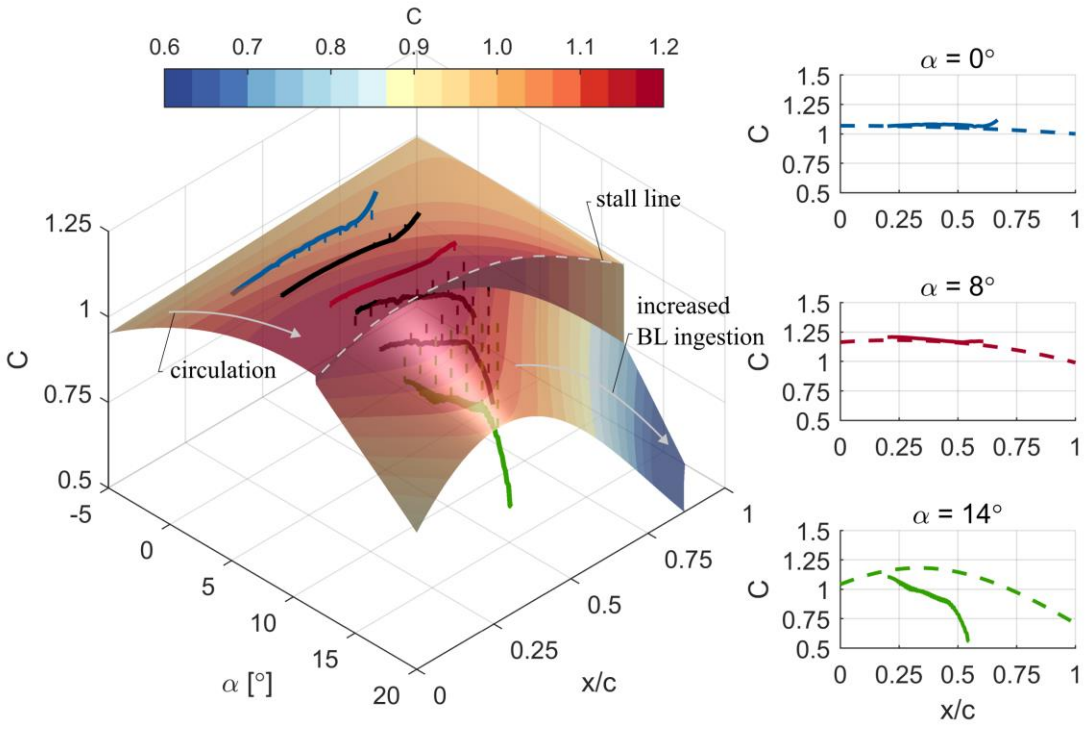

Figure 8 Left) Correction factor colored iso-surface for y/R = 0.27, including measurements from isolated wing as solid lines, right) comparison between model and isolated wind data for $\alpha = 0^o$, $\alpha = 8^o$ and $\alpha = 14^o$

The model response in Figure 8 shows an enhancement of the local advance ratio with increasing α by the circulation provided by the wing. This occurs up until $\alpha \approx 12^o$ which is the stall criterium of the current wing profile. Along the stall line a singularity is found, in which the correction factor C decreases by the separated boundary layer. In this regime, placing the propeller further backward will increase the amount of ingestion, explaining the downward trend in the direction of increasing x/c. On the right hand side of Figure 8, the measurements are compared to the model, represented by the dotted lines, for the three angles of attack. Advance ratio correction terms for $\alpha = 0^o$ and $\alpha = 8^o$ are modelled well, while there is a discrepancy between the model and measurements for $\alpha = 14^o$.

B. Propeller induced effects

The general flow features of the propeller-wing system are shown in Figure 9 by the velocity magnitude iso-contours and 2D velocity streamlines in a plane through the propeller axis. The non-uniform velocity pattern in the stream tube of the propeller is visible at a moderate angle of attack of $\alpha = 0^o$ in Figure 9a (see line A). Here, the velocity is higher near the surface of the wing as it approaches the propeller. Close to the propeller, the edge velocity decreases again and measurements indicate a flow separation region between the propeller and wing, indicated by point B. This is a known characteristics of installed propellers [17].

Increasing the angle of attack to $\alpha = 8^o$, more flow is induced by the wing, which is primarily visible close to the wing's leading edge in Figure 9b. Since the propeller is now positioned in an adverse pressure gradient, the separation region below the propeller moves forward, see point C. In Figure 9c, the wing-propeller system is under stall conditions, in which low momentum flow is ingested into the propeller. In these conditions the propeller also ingests flow downstream of the disk which can be seen in point D.

The induced velocity of the propeller V_i is visualized in Figure 9d, 9e and 9f by subtracting the isolated wing flow field from the installed flow field. Figure 9d shows a slight non-uniform induced velocity pattern caused by the

blockage of the contraction by the wing, allowing for larger velocities in point E. Upstream of the wing, the fluid is entrained in vertical direction, even though velocity magnitude is low. Propeller induced velocities are reduced for increased inclination in Figure 9e, indicating a reduction in thrust. In the post-stall region of Figure 9f, a complicated induced velocity field is found which does not represent the streamtube model. The small region of induced velocity near the leading edge (see point F) indicates limited stall delay provided by the propeller.

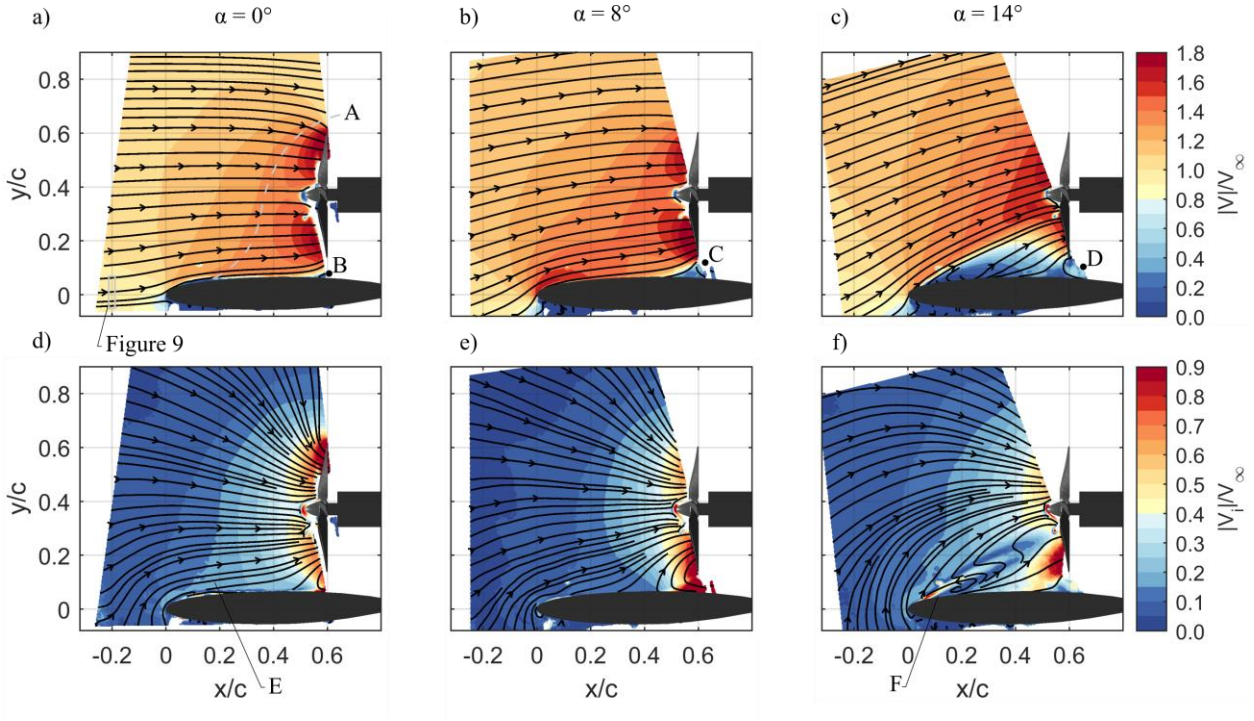

Figure 9) Top) Velocity magnitude contours and 2D streamlines for J = 0.3, for α = 0°, α = 8° and α = 14°, Bottom) Corresponding induced velocity magnitude contours and 2D streamlines

The velocity streamlines of Figure 9d, 9e and 9f indicate the velocities in vertical direction, creating an effective upwash for the wing. This effect is included in the lift model. It will be examined further by extracting vector properties upstream of the wing, indicated in Figure 9a, to estimate the increase in inflow angle $\Delta\alpha$ to the wing. The net increase $\Delta\alpha$ is presented for J = 0.3 and J = 0.6 for x_p/c = 0.6 in Figure 10a and x_p/c = 0.3 in Figure 10b. Note that the values for $\Delta\alpha$ are extracted from the plane through the propeller axes, and will therefore over predict the upwash for the full wing.

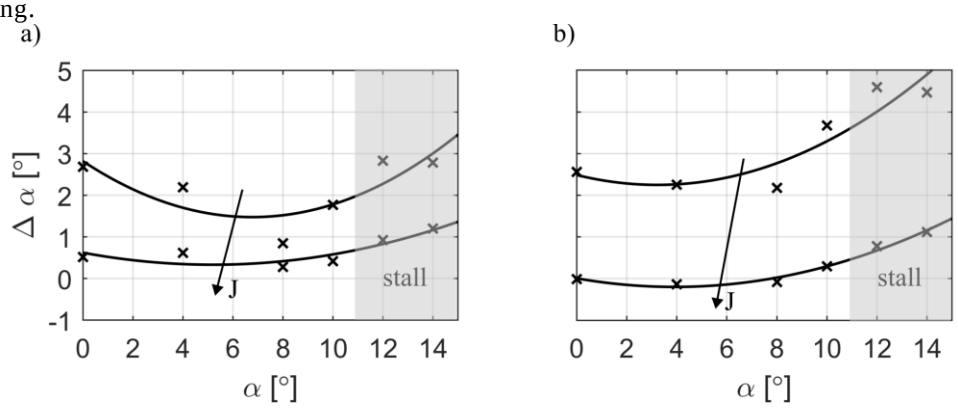

Figure 10 Increase in angle of attack $\Delta\alpha$ by propeller installation for J = 0.3 and J = 0.6 for x_p/c = 0.6 (a) and x_p/c = 0.3 (b). The solid line shows a 2nd order polynomial fit through the measurements.

In Figure 10a the effect of the radial induced velocity is shown through the increase in inflow angle. This effect is higher for the high thrust conditions, indicated by arrow which presents the trend for J. The upwash is reduced for increasing α in the pre-stall regime, but increases again after the boundary layer separates. By placing the propeller closer to the leading edge, in Figure 10b, the effect of the upwash is increased since stronger slipstream contractions are found closer to the propeller. Ultimately, these effects are captured in the model through $\Delta c_{l,\alpha}$, recall equation (4).

In the model, the axial induced velocity provided by the propeller follows from the actuator disk model and momentum equations. The validity of these approximations are examined using the induced velocity field from the measurements; i.e. the installed velocity field subtracted with the isolated wing velocity field. Attention will be paid to the non-uniformity and magnitude of the induced velocity, the properties of which are presented in Figure 11.

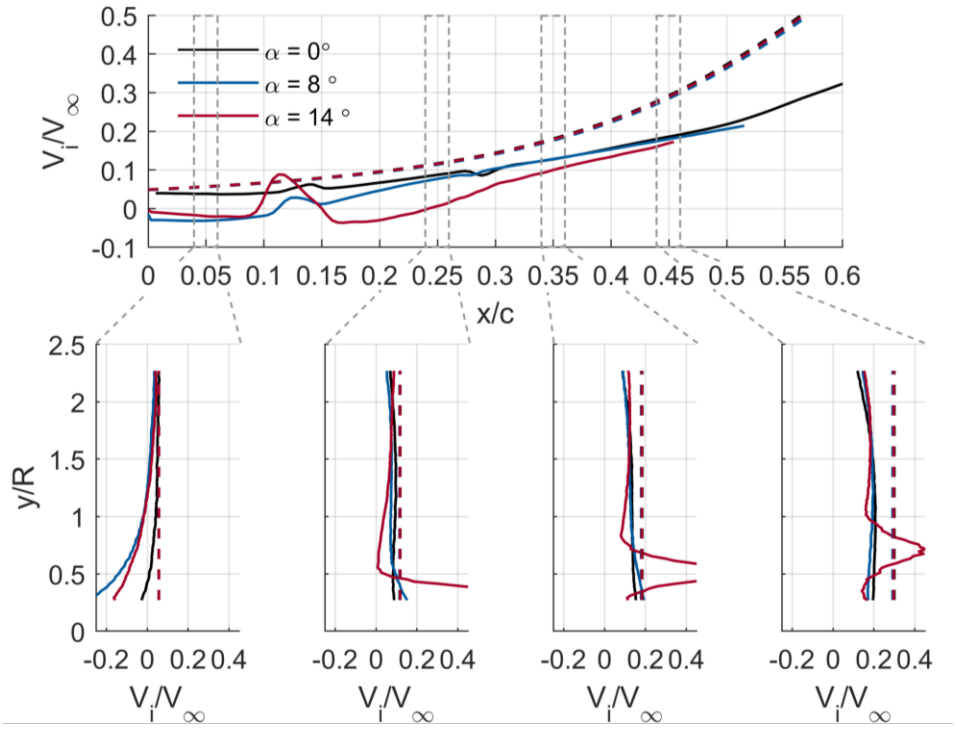

Figure 11 Top) propeller induced velocity upstream of the disk, bottom) non-uniformity in the stream tube at different chordwise positions for J = 0.3.

The top part of Figure 11 shows the chordwise distribution of the axial induced velocity, averaged over the disk for increasing inclination. The measurements, given by the solid lines show a clear reduction of axial induced velocity once the angle of attack is enhanced from 0º to 8º. When considering the boundary layer ingestion case of α = 14º, axial velocity is only induced after 0.25c (disregarding the hump around 0.125c which is an artefact of the boundary layer trip), which is after the boundary layer is separated. The lift model is based on an induced velocity and represented by the dotted lines in Figure 11. A slight over estimation of the induced velocity is found.

The bottom part of Figure 11 shows the non-uniformity of the induced velocity extracted at different chordwise positions. Typically, induced velocities are increased closer to the wing's surface which is not captured by the mode. As expected the case of α = 14º gives great non-uniformity in the induced velocity field since it accelerates the flow in the separated region.

C. Pressure distribution

It is expected that the suction provided by the propeller, as visualized in Figure 9, leads to a reduction of pressure upstream of the disk. Furthermore, a pressure increase after the propellers pressure jump is predicted. It is shown that the pressure orifices confirm this hypothesis for α = 0º, as is shown in Figure 12a which present the installed pressure distribution subtracted by the isolated wing data.

The data for α = 8º, however, present a different result. Here, a more pronounced pressure reduction is found at the suction peak compared to α = 0º. After this, the pressure is gradually increased to a maximum of $dc_p = 0.2$ at a position of x/c = 0.45, caused by the flow stagnation visualized in Figure 9b. Downstream of the disk, a reduction in pressure is found again. In the stall conditions of α = 14º there is a pressure reduction found in of all of the pressure taps along the suction side, with a stronger reduction between 0.4c and 0.6c by the suction inside the separated flow.

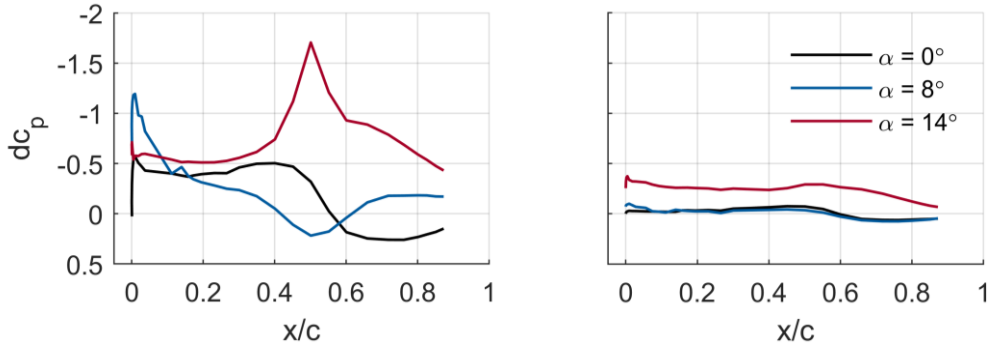

Figure 12 dC_p along the wing's suction side for different angles of attack, for J = 0.3 (left) and J =0.6 (right)

For the reduced thrust case of J = 0.6 in Figure 12b the effects of the propeller on the wing are minimized apart from α = 14º where a constant reduction of 0.3 is found for the pressure coefficient.

The measurements of Figure 12 only concerns the pressure taps below the propeller axis, while span wise variations are likely for the pressure field. The surface pressures over the wing at different spanwise positions are provided in Figure 13a and Figure 13b.

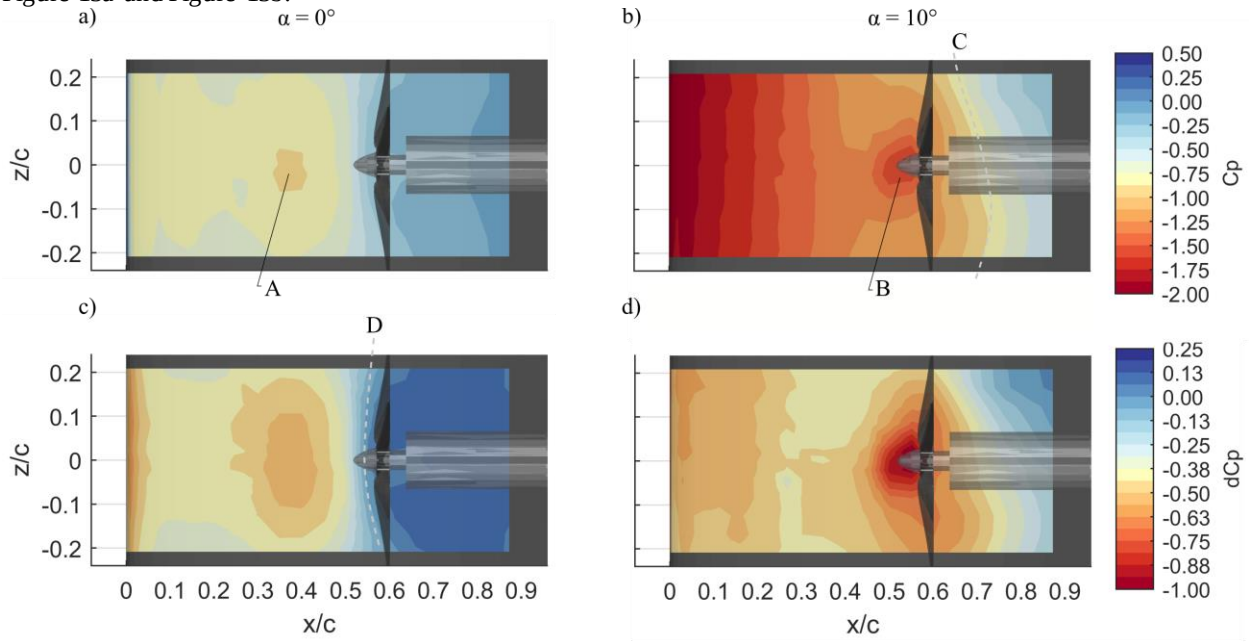

Figure 13 Surface Cp measurements and 2D velocity streamlines extracted 0.15c above the wing's surface for α = 0º (a) and α = 10º (b). c) and d) are similar to a) and b) but with the isolated wing pressure distribution subtracted.

For the data without inclination, presented in Figure 13a, the absolute value of the pressure is largest along the center span position and is gradually reduced by approximately 25% towards z/c = 0.2. Nonetheless, the surface pressure is

nearly perfectly symmetric along $z/c = 0$. The lowest pressure region is visible approximately $0.25c$ upstream of the disk, annotated by point A.

In Figure 13b the angle of attack is increased to $\alpha = 10^{o}$, the angle which provides the maximum lift for the isolated wing. The pressure reduction is obviously more pronounced near the leading edge by the increased circulation. Upstream of the propeller, little spanwise variations are found up. At point B, close to the propeller, a pressure reduction is found in the center span position. At this location variations in pressure with span are occurring, especially downstream of the propeller, indicated by line C.

By subtraction of the isolated wing's surface pressure, the effects of the propeller on the pressure distribution can be found in Figure 13c and Figure 13d. Pressure is reduced most significantly in the center span position. Line D presents the line in which the installed configuration's pressure distribution equals the isolated wing, i.e. $dc_p = 0$, and forms a parabolic line around the propeller.
For the case of $\alpha = 10^{o}$, the propeller induces spanwise variations in pressure over the entire measured surface. At the advancing side of the blade, i.e. positive z/c, the pressure by the propeller is slightly lower compared to the retreating side. Downstream of the propeller, pressures are higher at the retreating side.

VI. Trend analysis

Model results are presented in this chapter to properly understand the effect of inclination at different chordwise propeller positions, for various advance ratios. As validation, the results are also compared to the pressure and load measurements.

A. Propulsive thrust

Model predictions and measurements for the difference in thrust coefficient C_T compared to the isolated propeller are presented in Figure 14. For each of the propeller spacing a downward trend is visible for the thrust with increasing inclination. This decrease in thrust is more pronounced with the higher advance ratio, and when the propeller is positioned closer to the leading edge of the wing.
At the stall angle of the wing, i.e. $\alpha = 10^{o}$, the thrust increases again. Placing the propeller further towards the trailing edge increases the amount of re-ingestion, having a larger effect on the thrust increases.

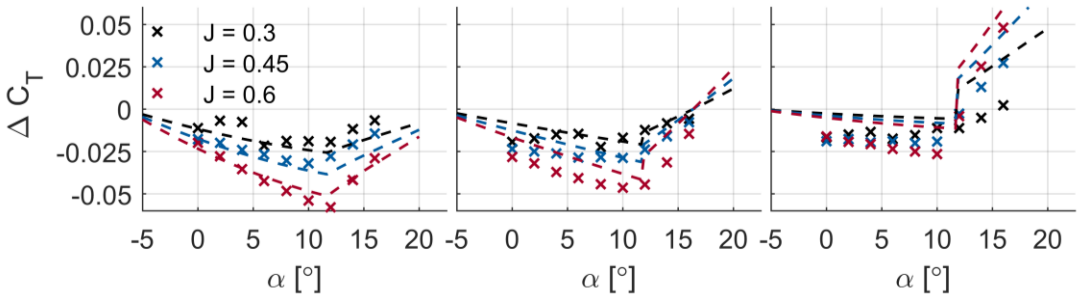

Figure 14 Difference in measured C_T for $x_p/c = 0.3$ (left), $x_p/c = 0.6$ (middle) and $x_p/c = 0.9$ (right). The dotted lines present the modelled trends.

The results of the model, given by the dashed lines, predict the trends in thrust well for the most forward propeller position. There are some discrepancies between the model and measurements once the propeller is closer towards the trailing edge, in the middle and right plot of Figure 14. The decrease of thrust with incidence angle is slightly underestimated. This is expected to be the resultant of the used wing model, which does not give a perfect parabolic pressure distribution. Additionally, since the stall criterium is a singularity in the model, this is also returned in the thrust results while the measurements results show a smoother pattern along stall conditions. Finally, the effect of ingestion is overpredicted for the propeller which is positioned close to the trailing edge, in right-hand side of Figure 14.

B. Wing lift

In the experiments, the lift coefficient c_l is estimated by integrating the static pressure measurements along the center span position. The results of the pressure distribution at different span positions in Section V.C shows that the effects of the propeller are most pronounced at this region. Hence, measured c_l will be overpredicted, but the information is still valuable to understand the trend behavior. Results for the measured and modelled lift are presented in Figure 15 for different advance ratios and propeller positions.

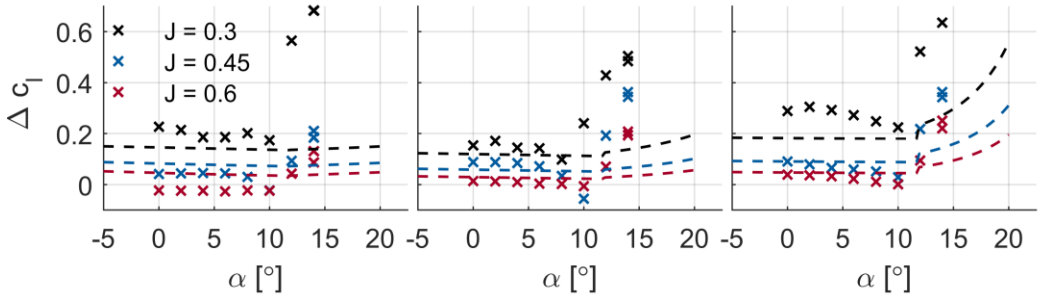

Figure 15 Difference in c_l derived from the pressure orifices for x_p/c = 0.3 (left), x_p/c = 0.6 (middle) and x_p/c = 0.9 (right). The dotted lines present the modelled trends.

The measurements shows a minor decreasing trend with α below the stall angle where the propeller position of x_p/c = 0.9 sees the largest enhancement of the lift, up to Δc_l = 0.3 for J = 0.3. In the post-stall regime, the lift enhancement is abruptly amplified, especially noticeable for the x_p/c = 0.3. The model underpredicts the lift enhancement for the high thrust case (J = 0.3), especially in the post-stall regime.

VII. Conclusions

The propeller's thrust is reduced when the propeller is positioned over the suction side of the wing. The difference compared to the isolated propeller depends on a combination of advance ratio, angle of attack and the chordwise position over the wing. In the pre-stall regime, thrust is reduced most significant for the propeller position near the wing's leading edge. After reaching the wing's stall angle, thrust is increased again by the ingestion of the separated boundary layer. These characteristics are captured by the semi-empirical model.

The induced flow of the propeller reduces the pressure on the suction side of the wing, leading to an increase in lift coefficient. This effect is most noticeable after reaching the stall angle. Here, the stall is not delayed but the lift increase is rather created by a result of an increase in effective inflow angle and the reduction of pressure inside the separated boundary layer.

The propeller's adverse pressure gradient also causes separation between the propeller and the wing. This separation region moves forward when the propeller is inclined. Close to stall, the propeller causes spanwise variations indicating complicated velocity field. Since the measured values of lift are based on the pressures in the center span position of the wing, below the propeller, these values are likely to be overpredicted. Hence, integral loading measurements of the wing are required to properly validate the lift predictions of the semi-empirical model.

Acknowledgments

This research is funded by the European Union's Horizon 2020 research and innovation programme, under grant agreement No. 860103, project ENODISE (Enabling optimized disruptive airframe-propulsion integration concepts). The authors would also like to acknowledge Tim Deleij and Laurens de Haan for their assistance during the experiments. Additional gratitude is given to Tom Lanters for the design of the propeller mounting.

References

[1] Thipphavong, David P., Rafael Apaza, Bryan Barmore, Vernol Battiste, Barbara Burian, Quang Dao, Michael Feary et al. "Urban air mobility airspace integration concepts and considerations." In *2018 Aviation Technology, Integration, and Operations Conference*, p. 3676. 2018.

[2] Borer, N. K., Patterson, M. D., Viken, J. K., Moore, M. D., Bevirt, J., Stoll, A. M., & Gibson, A. R. (2016). "Design and performance of the NASA SCEPTOR distributed electric propulsion flight demonstrator". In *16th AIAA Aviation Technology, Integration, and Operations Conference* (p. 3920).

[3] Johnson, W., Silva, C., and Solis, E., "Concept Vehicles for VTOL Air Taxi Operations," *Proceedings of the AHS Technical Conference on Aeromechanics Design for Transformative Vertical Flight*, American Helicopter Soc. International, Alexandria, VA, 2018

[4] Chauhan, S. S., & Martins, J. R. (2020). Tilt-wing eVTOL takeoff trajectory optimization. Journal of aircraft, 57(1), 93-112.

[5] Borer, N. K., Derlaga, J. M., Deere, K. A., Carter, M. B., Viken, S., Patterson, M. D., ... & Stoll, A. (2017). "Comparison of aero-propulsive performance predictions for distributed propulsion configurations". In *55th AIAA Aerospace Sciences Meeting* (p. 0209).

[6] Fredericks, W. J., McSwain, R. G., Beaton, B. F., Klassman, D. W., & Theodore, C. R. (2017). Greased lightning (GL-10) flight testing campaign (No. L-20737).

[7] Johnson, JR, J., & White, E. (1983, October). "Exploratory low-speed wind-tunnel investigation of advanced commuter configurations including an over-the-wing propeller design". In *Aircraft Design, Systems and Technology Meeting* (p. 2531).

[8] Grande, E., Romani, G., Ragni, D., Avallone, F., & Casalino, D. (2022). Aeroacoustic investigation of a propeller operating at low Reynolds numbers. *AIAA Journal*, 60(2), 860-871.

[9] Johnson, W., Silva, C., & Solis, E. (2018, January). Concept vehicles for VTOL air taxi operations. In AHS Specialists", *Conference on Aeromechanics Design for Transformative Vertical Flight* (No. ARC-E-DAA-TN50731).

[10] Tuck, E. O. (1991). A criterion for leading-edge separation. Journal of fluid mechanics, 222, 33-37.

[11] de Vries, R. (2022). Hybrid-Electric Aircraft with Over-the-Wing Distributed Propulsion: Aerodynamic Performance and Conceptual Design.

[12] Wick, A. T., Hooker, J. R., & Zeune, C. H. (2015). Integrated aerodynamic benefits of distributed propulsion. In 53rd AIAA Aerospace Sciences Meeting (p. 1500).

[13] Sinnige, T., De Vries, R., Corte, B. D., Avallone, F., Ragni, D., Eitelberg, G., & Veldhuis, L. L. (2018). Unsteady pylon loading caused by propeller-slipstream impingement for tip-mounted propellers. *Journal of Aircraft*, 55(4), 1605-1618.

[14] Avallone, F., Casalino, D., & Ragni, D. (2018). Impingement of a propeller-slipstream on a leading edge with a flow-permeable insert: A computational aeroacoustic study. *International Journal of Aeroacoustics*, 17(6-8), 687-711.

[15] Broadbent, E. G. (1976). Noise shielding for aircraft. Progress in Aerospace Sciences, 17, 231-268.

[16] Müller, L., Heinze, W., Kožulović, D., Hepperle, M., & Radespiel, R. (2014). Aerodynamic installation effects of an over-the-wing propeller on a high-lift configuration. *Journal of Aircraft*, 51(1), 249-258.

[17] de Vries, R., van Arnhem, N., Avallone, F., Ragni, D., Vos, R., Eitelberg, G., & Veldhuis, L. L. (2021). Experimental Investigation of Over-the-Wing Propeller–Boundary-Layer Interaction. *AIAA Journal*, 59(6), 2169-2182.

[18] Veldhuis, L. L. M. (2005). Propeller wing aerodynamic interference.

[19] Hanson, D. B. (1980). Helicoidal surface theory for harmonic noise of propellers in the far field. AIAA journal, 18(10), 1213-1220.

[20] Marcus, E. A., de Vries, R., Raju Kulkarni, A., & Veldhuis, L. L. (2018). Aerodynamic investigation of an over-the-wing propeller for distributed propulsion. *In 2018 AIAA Aerospace Sciences Meeting* (p. 2053).

[21] Murray, H. H., Devenport, W. J., Alexander, W. N., Glegg, S. A., & Wisda, D. (2018). Aeroacoustics of a rotor ingesting a planar boundary layer at high thrust. *Journal of Fluid Mechanics*, 850, 212-245.

[22] De Vries, R. (2022). Hybrid-Electric Aircraft with Over-the-Wing Distributed Propulsion: Aerodynamic Performance and Conceptual Design.

[23] Viterna, L. A., & Corrigan, R. D. (1982). Fixed pitch rotor performance of large horizontal axis wind turbines. *Large Horizontal-Axis Wind Turbines*, NASA CP-2230, 1982, pp.69-86.

[24] Tuck, E. O. (1991). A criterion for leading-edge separation. *Journal of fluid mechanics*, 222, 33-37.

[25] Murphy, J. P., & MacManus, D. G. (2011). Inlet ground vortex aerodynamics under headwind conditions. *Aerospace science and technology*, 15(3), 207-215.

[26] Yang, Y., Sciacchitano, A., Veldhuis, L. L. M., & Eitelberg, G. (2016). Spatial-temporal and modal analysis of propeller induced ground vortices by particle image velocimetry. *Physics of Fluids*, 28(10), 105103.